Effect of metastable oxygen molecules in high density power-modulated oxygen discharges

Siddhartha Panda and Demetre J. Economou[a]
Plasma Processing Laboratory, Department of Chemical Engineering, University of Houston, Houston, Texas 77204-4792

M. Meyyappan
NASA Ames Research Center, Moffett Field, California 94035

A spatially averaged (well mixed) reactor model was used to simulate a power-modulated (pulsed) high density oxygen discharge. Chemistry involving the high energy oxygen metastable molecules $O_2^M(A\,^3\Sigma_u^+ + C\,^3\Delta_u + c\,^1\Sigma_u^-)$ was included in the simulation. This chemistry was necessary to capture the experimentally observed increase in the O^- negative ion density in the afterglow of the pulsed discharge. As the electron temperature drops in the afterglow, the rate coefficient of electron attachment with O_2^M increases several fold. The wall recombination probability of oxygen atoms affected the O^- density drastically. For the conditions studied, the maximum O^- density in the afterglow increased with pressure, decreased with power, and showed a maximum with pulse period. The time in the afterglow at which the peak O^- density occurred decreased with pressure and power, and was independent of the pulse period. Knowing the temporal evolution of O^- in the afterglow may be important for applications requiring extraction of negative ions out of the discharge. © *2000 American Institute of Physics.* [S0021-8979(00)07512-5]

I. INTRODUCTION

Power modulated discharges have been used to obtain higher deposition rate and better quality of hydrogenated silicon films by plasma enhanced chemical vapor deposition[1–3] as well as suppression of particulates.[1,2,4] In addition, it has been found that, for small pulse widths, the silicon etch rate in power modulated plasmas is similar to that in continuous wave (cw) discharges, thereby obtaining a higher etch rate for the same average power.[5–7] Law *et al.*[8,9] also found higher GaAs etch rate for small pulse widths. Boswell and Henry[6] found that for a constant average rf power, the selectivity of etching Si over SiO$_2$ can be varied from 6 to 100 by reducing the pulse period while keeping a constant duty ratio. Samukawa and Furoya[10–12] used a pulsed CHF$_3$ high density discharge to control polymerization during SiO$_2$ etching by controlling the generation of the reactive species to obtain high anisotropy, selectivity, and elimination of microloading. Takahashi *et al.*,[13] also using a pulsed CHF$_3$ high density plasma, obtained controlled deposition of fluorocarbon films by controlling the reactive species concentration. Fujiwara *et al.*[14] reported notch depth reduction in power modulated Cl$_2$ and HCl plasmas, depending on the duration of the discharge ''off'' time. Selective, anisotropic, and notch-free polycrystalline silicon etching was obtained in power modulated chlorine plasmas,[15,16] by controlling the ion energy distribution through the duty ratio, having a high ion flux, and apparently eliminating charging by alternate bombardment of the wafer by positive and negative ions. Pulsed plasmas have also been used for negative ion sources.[17]

Plasma rector modeling helps understand the underlying mechanisms and the effect of various process parameters. Several modeling studies of pulsed plasmas have been reported in the literature. Park and Economou[18] used a one-dimensional (1D) axial dispersion model to analyze a pulsed plasma-enhanced chemical vapor deposition reactor. They found that, by selection of appropriate values of the pulse period and duty ratio, uniformity could be improved without significant reduction in deposition rate. Similar findings were reported for an etching reactor.[19] Jiang *et al.*[20] found that pulsing can alter the ratio of chemical species in CF$_4$ discharges, which in turn can affect etch selectivity. Overzet and co-workers[21,22] used a 1D fluid model for the electric field and particle densities in the afterglow of an rf discharge. They found that the attachment rate in the afterglow influenced the time dependence of the negative ion flux. Peres and Pitchford[23] presented results from 1D and two-dimensional (2D) models to illustrate a type of attachment instability which can occur in glow discharges in electronegative gas mixtures. Lymberopoulos *et al.*[24] used a 1D fluid model to investigate the spatiotemporal dynamics of a pulsed power inductively coupled plasma (ICP) argon plasma. Attention was paid to the extraction and acceleration of positive ions by an rf bias applied in the afterglow stage of the pulsed discharge. Midha and Economou[25] extended the spatially resolved simulation to electronegative plasmas. Smith *et al.*[26] used a 1D particle-in-cell simulation to investigate the effect of pulsing on a low pressure capacitively coupled rf argon plasma. Yokozawa *et al.*[27] studied a pulsed Cl$_2$ plasma using the Monte Carlo method and discussed the contribution of negative ions to etching. Using a Monte Carlo technique, Hwang and Giapis[28] studied high density pulsed plasmas and

[a]Electronic mail: economou@uh.edu

suggested a mechanism for pattern dependent charging, based on the low energy part of the energy distribution of positive ions. Spatially averaged models have been used to study cw discharges in oxygen[29] and chlorine[30] and pulsed discharges in chlorine,[31,32] argon,[33] and SF_6[34] gases. Oxygen plasmas are used in the microelectronics industry for etching of photoresist[35] and other polymers, for plasma oxidation and cleaning.[36]

In this work, a spatially averaged (well mixed) model of a high density power modulated (pulsed) oxygen discharge was developed. Special attention was paid to the effect of high energy metastable oxygen molecules on the discharge characteristics, especially the negative ion density. This study was motivated by the experimental findings of Hayashi and Kadota[37] who observed a large increase in the negative oxygen ion (O^-) density in the afterglow of a pulsed oxygen discharge. Their experimental data could be explained by including dissociative attachment of electrons to high energy metastable oxygen molecules $O_2^M(A\,{}^3\Sigma_u^+ + C\,{}^3\Delta_u + c\,{}^1\Sigma_u^-)$. Our simulation results, which include new chemistry to account for such metastable molecules, are consistent with their experimental findings. The increase in O^- in the afterglow cannot be captured using the traditional oxygen chemistry employed so far in the literature. The new chemistry is useful for optimizing the O^- concentration and flux in pulsed oxygen discharges and for basic oxygen plasma kinetic studies.[38]

II. MODEL

The model provides for the analysis of a generic "high density" plasma reactor. Spatially averaged (well mixed) models provide the average species concentration and cannot provide information on the spatial profiles and process uniformity as would multidimensional models. The advantage of spatially averaged models is that they are solved with minimum computational resources. They provide a quicker path to studying the effect of process variables (power, pressure etc.), and complicated chemistry can be included.[39] Insight from spatially averaged models can be used in developing more rigorous multidimensional models. The plasma chamber considered here is a cylinder of radius R and length L. Details of the model are given in the SAMPR Manual.[40]

A. Species mass conservation

The mass balance for the ionic and neutral species is written as

$$\rho V \frac{dy_i}{dt} = \dot{m}(y_{i,in} - y_i) + VM_i\sum_j R_{ij} + AM_i\sum_k S_{ik}, \quad i=1,I,$$
(1)

where I is the total number of ionic and neutral species. ρ is the mass density of the mixture, y_i is the mass fraction of species i (with the subscript in referring to the inlet conditions), $\dot{m}$ is the total mass flow rate, M_i is the molecular mass of species i, V is the reactor volume, and A is the surface area. R_{ij} is the molar homogeneous reaction of species i in reaction j and S_{ik} is the molar heterogeneous reaction of species i in reaction k. The three terms on the right hand side

(rhs) of Eq. (1) represent change due to flow, volume, and surface reactions, respectively. The homogeneous reaction rate R_{ij} is written as

$$R_{ij} = (\nu_{ij}'' - \nu_{ij}')\left[k_{fj}\prod_{i=1}^{i=I} (\rho y_i/M_i)^{\nu_{ij}'} - k_{rj}\prod_{i=1}^{i=I} (\rho y_i/M_i)^{\nu_{ij}''} \right],$$
(2)

where ν_{ij} is the stoichiometric coefficient of species i in reaction j, with the single and double primes denoting reactants and products, respectively. k_{fj} and k_{rj} are the forward and reverse rate coefficients, respectively, for reaction j.

The plasma is assumed to be neutral and the electron number density is obtained from

$$n_e = \sum_{i=1}^{I} q_i n_i,$$
(3)

where q_i is the charge of species i.

B. Thermodynamic relation

The overall gas density, ρ, is calculated from

$$p = \sum_{i \neq e} p_i + p_e,$$
(4)

$$= R_g T_g \rho\left[\sum_{i \neq e} \frac{y_i}{M_i} + \frac{T_e}{T_g}\frac{y_e}{M_e} \right],$$
(5)

where p is the total reactor pressure, R_g is the universal gas constant, and T_e is the electron temperature. In principle, the contribution of the ion temperature can be incorporated in Eq. (5) separately, but its effect is negligible. Here, the ion temperature is assumed to be the same as the gas temperature (T_g).

C. Power balance

Plasma power is treated as an input variable. In this spatially averaged model, the nature of power deposition, magnetic fields effects, etc., are not included. Assuming a Maxwellian electron energy distribution function (EEDF), the power balance in the plasma is of the form

$$1.5V\frac{d(n_e k T_e)}{dt} = P_{\text{ext}} - P_e - P_+ - P_-,$$
(6)

where the rhs terms are the externally applied power, and energy losses (per unit time) by electrons, positive ions, and negative ions, respectively. Assuming the electron-ion volume recombination to be negligible, P_e is obtained from

$$(Qn_e\varepsilon_e)_{\text{in}} - Qn_e\varepsilon_e + P_e - VN\sum_j R_{ej}H_j$$

$$- 3\left(\frac{m_e}{m}\right)\nu_{el}Vn_e k(T_e - T_g) - 2kT_e A\Gamma_e = 0.$$
(7)

Q is the total flow rate given by $\dot{m}/\rho, \varepsilon_e$ is the mean electron thermal energy ($=3/2\ kT_e, k$ being the Boltzmann constant), N is the Avogadro number, R_{ej} is the rate of electron impact reaction j, H_j is the corresponding threshold energy, m is the mixture average mass, v_{el} is the electron elastic collision

frequency, and Γ_e is the electron wall flux. The terms in Eq. (7) represent electron energy inflow and outflow due to gas flow, energy gain from the external power source, and energy loss due to inelastic collisions, elastic collisions, and wall recombination of electrons, respectively. The electron flux to the wall is given by

$$\Gamma_e = (A_{\text{eff}}/A)(n_e/4)v_{e,\text{th}}\exp(-\Delta\Psi/kT_e), \quad (8)$$

where $\Delta\Psi$ is the sheath potential equal to the difference between the plasma and wall potentials and $v_{e,\text{th}} = (8kT_e/\pi m_e)^{0.5}$ is the electron thermal velocity. A_{eff} is an effective area to account for the deviation of sheath edge ion density from that at the discharge center

$$A_{\text{eff}} = A_R h_R + A_L h_L, \quad A = A_R + A_L \quad (9)$$

with A_R and A_L being the areas of the radial and axial sheaths, respectively.

The correction factors h_R and h_L are[41]

$$h_L = \frac{n_{+sL}}{n_{+0}} \approx \frac{1+\dfrac{2\alpha_s}{\gamma_T}}{1+\alpha_s}0.86\left[3+\frac{L}{2\lambda_i}+\left(\frac{0.86Lu_B}{\pi\gamma_T D_i}\right)^2\right]^{-1/2}, \quad (10)$$

$$h_R = \frac{n_{+sR}}{n_{+0}} \approx \frac{1+\dfrac{3\alpha_s}{\gamma_T}}{1+\alpha_s}0.80\left[4+\frac{R}{\lambda_i}\right.$$
$$\left. +\left(\frac{0.8Ru_B}{2.405J_1(2.405)\gamma_T D_i}\right)^2\right]^{-1/2}, \quad (11)$$

where λ_i is the ion mean free path based on ion–neutral collisions. The ion diffusion coefficient is $D_i = kT_i/(m_+\nu_i)$, m_+ is the ion mass and ν_i is the ion–neutral collision frequency. The electronegativity of the plasma, α_s, is defined as the ratio of the negative ion density to electron density at the sheath edge. γ_T is the ratio of the electron temperature to the ion temperature, J_1 is a Bessel function, and u_B is the Bohm velocity (see below).

The power lost by positive ions is

$$P_+ = A\Gamma_+\Delta\Psi, \quad (12)$$

where the positive ion flux, Γ_+, is

$$\Gamma_+ = (A_{\text{eff}}/A)\sum n_+ u_B. \quad (13)$$

n_+ being the positive ion density, and the summation is over all positive ions. The Bohm velocity for electronegative gases is given by[42]

$$u_B = \left[\frac{kT_e(1+\alpha_s)}{m_+(1+\alpha_s\gamma_T)}\right]^{1/2}. \quad (14)$$

The power lost by negative ions is

$$P_- = 2kT_i A\Gamma_-, \quad (15)$$

where the negative ion flux is

TABLE I. Reactions and rate coefficients (cc/s).

1	$e+O_2>O_2+e$:	$4.7\times10^{-8}\,T_e^{0.5}$
2	$e+O_2>O^-+O$:	$8.8\times10^{-11}\exp(-4.4/T_e)$
3	$e+O_2>2O+e$:	$2.6\times10^{-8}\exp(-9.97/T_e)$
4	$e+O_2>O_2^++2e$:	$9.0\times10^{-10}\,T_e^{0.5}\exp(-12.6/T_e)$
5	$e+O^->O+2e$:	$2.0\times10^{-7}\exp(-5.5/T_e)$
6	$e+O_2^+>2O$:	$5.2\times10^{-9}/T_e$
7	$O^-+O_2^+>O+O_2$:	$2\times10^{-7}(300/T)^{0.5}$
8	$O^-+O>O_2+e$:	5×10^{-10}
9	$O^-+O_2^+>3O$:	1×10^{-7}
10	$e+O_2>O^-+O^++e$:	$7.1\times10^{-11}\,T_e^{0.5}\exp(-17/T_e)$
11	$e+O_2>O+O^++2e$:	$5.3\times10^{-10}\,T_e^{0.9}\exp(-20/T_e)$
12	$e+O>O^++2e$:	$9.0\times10^{-9}\,T_e^{0.7}\exp(-13.6/T_e)$
13	$O^-+O^+>2O$:	$2\times10^{-7}(300/T)^{0.5}$
14	$O^++O_2>O+O_2^+$:	$2\times10^{-11}(300/T)^{0.5}$
15	$e+O_2>O_2^*+e$:	$1.7\times10^{-9}\exp(-3.1/T_e)$
16	$e+O_2^*>O_2+e$:	$5.6\times10^{-9}\exp(-2.2/T_e)$
17	$O_2^*+O_2>2O_2$:	$2.2\times10^{-18}(300/T)^{0.8}$
18	$O_2^*+O>O_2+O$:	1×10^{-16}
19	$e+O_2>O+O^*+e$:	$5.0\times10^{-8}\exp(-8.4/T_e)$
20	$e+O>O^*+e$:	$4.2\times10^{-9}\exp(-2.25/T_e)$
21	$e+O^*>O+e$:	8×10^{-9}
22	$e+O^*>O^++2e$:	$9\times10^{-9}\,T_e^{0.7}\exp(-11.6/T_e)$
23	$O^*+O>2O$:	8×10^{-12}
24	$O^*+O_2>O+O_2$:	$7\times10^{-12}\exp(67/T)$
25	$O^*+O_2>O+O_2^*$:	1×10^{-12}
26	$O^-+O_2>O_3+e$:	5×10^{-15}
27	$e+O_3>O_2^-+O$:	1×10^{-9}
28	$O^-+O_2^*>O_3+e$:	3×10^{-10}
29	$O^-+O_2^*>O_2^-+O$:	1×10^{-10}
30	$O_2^-+O_2^+>2O_2$:	$2\times10^{-7}(300/T)^{0.5}$
31	$O_2^-+O^+>O_2+O$:	$2\times10^{-7}(300/T)^{0.5}$
32	$O_3+O_2>O_2+O+O_2$:	$7.3\times10^{-10}\exp(-11\,400/T)$
33	$O_3+O>2O_2$:	$1.8\times10^{-11}\exp(-2300/T)$
34	$e+O_2^*>O^-+O$:	$3.53\times10^{-9}\,T_e^{-1.46}\exp(-5.35/T_e)$
35	$e+O_2>O_2^M+e$:	$1.27\times10^{-8}\,T_e^{-0.52}\exp(-7.66/T_e)$
36	$e+O_2^M>O^-+O$:	$-1.69\times10^{-12}+6.27\times10^{-10}/T_e$ $-1.30\times10^{-10}/T_e^2+9.60\times10^{-12}/T_e^3$
37	$e+O_2^M>2O+e$:	$8.95\times10^{-9}\,T_e^{-0.48}\exp(-4.32/T_e)$

$$\Gamma_- = \frac{\alpha_s}{1+\alpha_s}(\Sigma n_+)(A_{\text{eff}}/A)(1/4)v_{-,\text{th}}\exp(-\Delta\Psi/kT_i) \quad (16)$$

and $v_{-,\text{th}}$ is the thermal velocity of negative ions.

III. CHEMISTRY

A. Gas phase reactions

The set of gas phase reactions used in the model is shown in Table I. Reactions 1–2 and 4–33 are taken from the text of Lieberman and Lichtenberg.[42] Rate coefficients for reactions 3 and 34–37 are calculated as part of this work. The species used are O, O^+, O^-, O_2, O_2^+, O_2^-, O_3, and the metastables $O^*(^1D)$, $O_2^*(a\,^1\Delta_g)$ and $O_2^M(A\,^3\Sigma_u^+ + C\,^3\Delta_u + c\,^1\Sigma_u^-)$. Three body collisions were neglected because of the low pressure system considered.

The dissociative attachment cross section for O_2^* as given by Burrow[43] was used to calculate the rate coefficient (K) for reaction 34 by assuming a Maxwellian EEDF
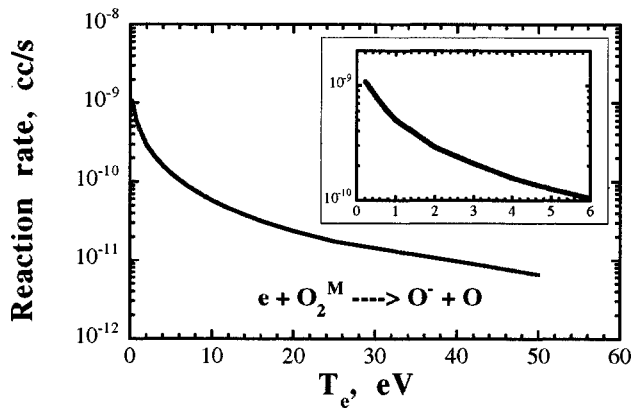
FIG. 1. Rate coefficient for dissociative electron attachment to O_2^M metastable oxygen molecules (reaction 36 of Table I) as a function of electron temperature.

$$K = \sqrt{\frac{8}{\pi m_e}} \int_0^\infty \sigma(\varepsilon) \frac{\exp(-\varepsilon/kT_e)}{(kT_e)^{3/2}} \varepsilon\, d\varepsilon, \qquad (17)$$

where ε is the electron energy and $\sigma(\varepsilon)$ is the collision cross section.

The rate coefficient for production of O^- by reactions 2 and 34 (Table I) decreases monotonically with decreasing T_e. Apparently, these reactions alone cannot account for the experimentally observed large increase of O^- in the late afterglow of pulsed oxygen discharges. To explain the experimental data, Hayashi and Kadota[37] proposed dissociative attachment of electrons to the highly excited metastable states $O_2^M(A\,^3\Sigma_u^+ + C\,^3\Delta_u + c\,^1\Sigma_u^-)$ to form O^-. This is represented by reaction 36 in Table I. As these metastable states are located about 4 eV above the ground state $O_2(X\,^3\Sigma_g^+)$, it is expected that the threshold energy for dissociative attachment to O_2^M will be lower than that to ground state oxygen. For O_2^*, the corresponding threshold energy is lower by about 1 eV and the peak cross section is about 3.5 times higher than that of ground state O_2. The peak dissociative attachment cross-section for O_2^M is likewise expected to be higher compared to that for ground state oxygen. Dissociative attachment of low energy electrons to O_2^M is proposed to be via the formation of a complex state $[O_2^-]^*$, for example $O_2^-(^2\Pi_u)$, by the resonant capture of an electron. The dissociative attachment cross-section data from Hayashi and Kadota[44] is used for O_2^M. The corresponding rate coefficient is shown in Fig. 1 as a function of T_e.

Cross-section data of Teillet–Billy et al.[45] and Itikawa et al.[46] were used to evaluate the rate coefficient for the production of O_2^M by electron impact excitation. Besides dissociative attachment, the O_2^M metastables are also destroyed by electron impact dissociation (reaction 37 in Table I). As no data is available for the dissociation of O_2^M, the O_2^M excitation cross-section was used to calculate the dissociation rate coefficient, with the energy scale shifted down by 4 eV. The rate coefficients for reactions 35–37 were calculated the same way as for reaction 34 [Eq. (17)]. Expressions were fitted to these data as given in Table I. (The R values of the fits were all greater than 0.999.)

For dissociation of O_2 molecules, Itikawa et al. used[46]

$$Q_{\mathrm{dis}} = Q_{\mathrm{ex}}(B\,\Sigma_u^-) + Q_{\mathrm{ex}}(O_2^M), \qquad (18)$$

where Q_{diss} is the dissociation cross-section. However, since we account for dissociation of O_2^M in reaction 37, only dissociation through the $B\,^3\Sigma_u^-$ state is considered in reaction 3. The fit for reaction 3 (with R value greater than 0.999) is also given in Table I.

B. Surface reactions

Surface reactions used here involve simple collision of atomic, molecular, or ionic species, resulting in products. The rate coefficient (cm/s) is specified or calculated from

$$k_{si} = \gamma_i \sqrt{\frac{R_g T_g}{2\pi M_i}}, \qquad (19)$$

where γ_i is an effective reaction probability, accounting for rarefaction effects near the wall (see Ref. 47). A reaction probability of 1 was used for O^*, and zero for O_3. A value of 10^{-5} was used for $O_2^{*\,43,48}$ and the same value was used for O_2^M. For oxygen atoms, Bell[49] gives a value of 0.002 to 0.03 which is typical for quartz. A value of 0.01 was used here as the base value for O atom recombination on the walls. However, the effect of varying the value of γ for O-atom recombination was studied. Ionic species were assumed to completely neutralize at the wall.

IV. RESULTS AND DISCUSSION

A. Comparison with experimental data

1. Pulsed plasma

Hayashi and Kadota[37] measured the O^- negative ion concentration in high density pulsed oxygen plasmas. They used a quartz discharge tube, 3 cm in inside diameter and 25 cm in length. The discharge conditions were: O_2 flow rate of 10 sccm, rf power of 0.65–1 kW, gas pressure of 5 mTorr, discharge duration (plasma "on" time) of 0.7–10 ms and repetition rate of 5 Hz (i.e., a pulse period of 200 ms). Before comparing our calculated results with their data, we plot in Fig. 2 the O^- density and electron density, as a function of γ for O-atom wall recombination, in a steady-state discharge at 800 W (other conditions as stated above). The calculated O^- density depends on the value of the O-atom wall recombination coefficient (γ). Larger γ result in higher O^- concentration, as the O_2 and O_2^M concentrations also increase. In the range $\gamma = 0.01–0.4$, the O^- density increases by more than an order of magnitude from 4.8×10^8 to 5.1×10^9/cc. On the other hand, for this weakly electronegative system, the electron density decreases by only 15% (2.8×10^{12} to 2.4×10^{12}/cc) in the same γ range.

High γ values (≈ 0.5) are associated with stainless steel[50] and are generally believed to be unrealistic for quartz. However, Matsushita et al.[51] measured the recombination coefficient of O atoms on their quartz chamber wall using two-photon laser induced fluorescence in a high density helicon-wave excited oxygen plasma. They found the coefficient to be a strong function of the discharge conditions and obtained values of 0.1–1. Collart et al.[52] commented about the presence of a heated teflon holder in the oxygen plasma experiments of Cook and Benson[53] which was thought to be
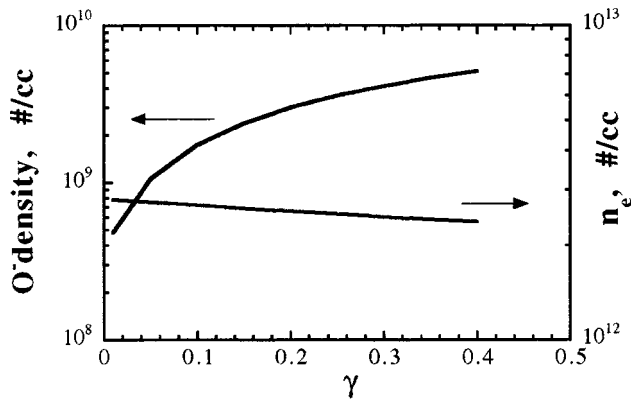
J. Appl. Phys., Vol. 87, No. 12, 15 June 2000

Panda, Economou, and Meyyappan   8327

FIG. 2. O^- and electron densities for different values of the wall recombination probability of O atoms (γ) for a steady-state oxygen plasma at 10 sccm, 5 mTorr, and 800 W.

a source of fluorine; fluorine has been found to increase γ in oxygen plasmas.[38] Tserepi and Miller[38] found γ to increase with power and decrease with pressure under the conditions used in their rf oxygen plasma reactor. The conclusion is that an accurate value of γ is difficult to obtain, since γ may change even as the reactor operating conditions vary.

Figure 3 shows the experimentally measured[37] O^- concentration in the afterglow of a pulsed oxygen plasma at 5 mTorr, 10 sccm pure oxygen flow and 800 W. The measured O^- concentration when power was turned off is 10^{11}/cc. The O^- concentration peaks at about 15 μs in the afterglow to 5.4×10^{11}/cc and then decreases. Simulated results, using $\gamma = 0.01$, 0.1, and 0.4, for the same conditions as in the experiment are also shown in Fig. 3. The trend in the simulated O^- concentration is similar to the experimental data, with the O^- density having a peak 13–16 μs into the afterglow, and with the peak concentration about 7 times higher than that at power off. Higher γ values result in faster decay of O^- after reaching the peak. Another factor affecting the O^- concentration is the input power. The actual power dissipated in the plasma could be much lower than the metered power because of power losses. Schwabedissen et al.[54] for example, found the dissipated power to be 27%–64% of the incident power
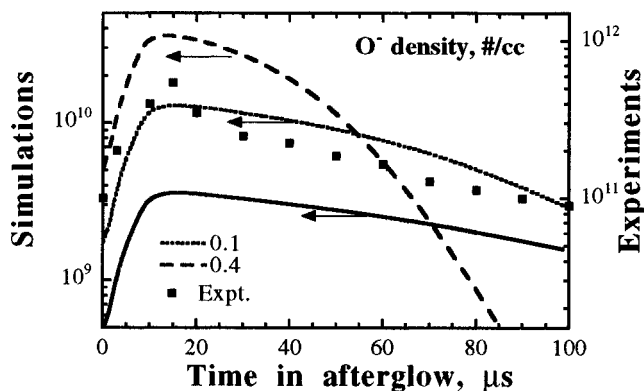

FIG. 3. Comparison of simulated O^- densities in the afterglow of a pulsed oxygen plasma (lines) with experimental data (points) of Hayashi and Kadota (Ref. 37). Conditions were: 10 sccm, 5 mTorr, and 800 W. Simulations are shown for three different values of the wall recombination probability of oxygen atoms, γ.
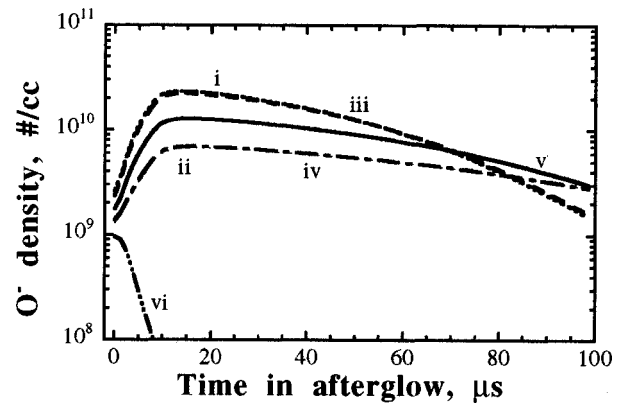

FIG. 4. Sensitivity of O^- density in the afterglow of a pulsed oxygen discharge to reaction rate coefficients: (i) coefficient of reaction 35 (Table I) multiplied by 2, (ii) coefficient of reaction 35 divided by 2, (iii) coefficient for reaction 36 multiplied by 2, (iv) coefficient of reaction 36 divided by 2, and (v) coefficient of reactions 35 and 36 as given in Table I. O^- density evolution without including O_2^M in the chemistry of Table I is shown as curve (vi). Other conditions were: 10 sccm, 5 mTorr, 800 W, $\gamma = 0.1$.

in their inductively coupled oxygen plasma at 20 mTorr. A lower power into the plasma would result in lower O_2 dissociation and hence a higher O^- concentration. Decreasing the power to 400 W in the simulations (i.e., assuming that only 50% of the input power is dissipated in the plasma), with $\gamma = 0.01$, resulted in an O^- concentration of 8.8×10^8/cc at power turn off (instead of 4.8×10^8/cc at 800 W of power). Under these conditions, the peak concentration was 6.7 times this value and occurred 17 μs into the afterglow.

The sensitivity of the results to the reaction rate coefficient (K) for formation of O_2^M (reaction 35 of Table I) and dissociative attachment of O_2^M (reaction 36) was studied. With γ at 0.1, the O^- density is shown in Fig. 4 with (i) K for reaction 35 multiplied by 2, (ii) K for reaction 35 divided by 2, (iii) K for reaction 36 multiplied by 2, and (iv) K for reaction 36 divided by 2. The O^- profile for the reaction rates of Table I is also shown for comparison (v). Plots for cases (i) and (iii) almost overlap. An overlap is also seen for cases (ii) and (iv). At power turn off, the O^- densities are 2.4×10^9, 1.4×10^9, 2.6×10^9, 1.3×10^9, and 1.7×10^9/cc, for cases (i)–(v), respectively. Thus a change in these reaction rates by a factor of 2 results in a change of O^- density by a factor of less than two. Also shown in Fig. 4 is the O^- density evolution without taking into account the O_2^M species (vi). Without the O_2^M species, the O^- density decays rapidly after power turn off and does not show a peak as observed experimentally.[37]

Figure 5 shows the electron density for the same conditions as for Fig. 3, but with $\gamma = 0.01$ only. The simulated electron density at power off is 2.8×10^{12}/cc, 3.1 times the experimentally measured value of 9.0×10^{11}/cc. Decreasing the power to 400 W (to account for possible power losses), resulted in an electron density of 1.4×10^{12}/cc at plasma off, closer to the experimental value.

2. Steady state plasma

The oxygen atom concentration predicted by the model for a steady state oxygen plasma at 350 W for different pres-
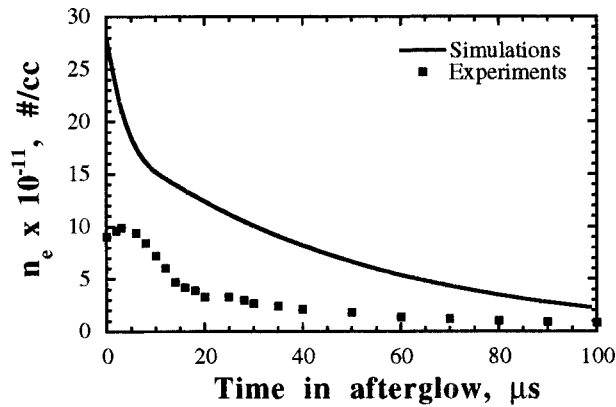
FIG. 5. Comparison of simulated electron density in the afterglow of a pulsed oxygen plasma (line) with experimental data (points) of Hayashi and Kadota (see Ref. 37). Conditions were: 10 sccm, 5 mTorr, 800 W, γ = 0.01.

sures (20–50 mTorr) is shown in Fig. 6. The O atom concentration is seen to increase with pressure at these conditions. Optical emission actinometry with argon as an actinometer was used to measure the relative O atom concentration by normalizing the 844 nm O peak with the 750 nm Ar peak. The experimental values, normalized to the value obtained from the model at 30 mTorr, are shown in the same figure. The behavior of the experimental results matches reasonably well with those obtained from the model.

B. Parametric analysis

With the model having successfully captured the experimental trends, a parametric analysis is conducted to study the effect of operating conditions on plasma properties. For this study we used a cylindrical quartz plasma reactor of radius 3.175 cm and length 25 cm. We used a gas temperature of 400 K and a flow rate of 10 sccm of pure oxygen. The base case conditions are given in Table II. Power is modulated by ideal rectangular pulses having zero rise and fall times:

$$P(t) = 0, \quad d \times \tau \leqslant t < \tau,$$

where d is the duty ratio, τ is the pulse period, and t is time. Figures below show results corresponding to one cycle (nor-
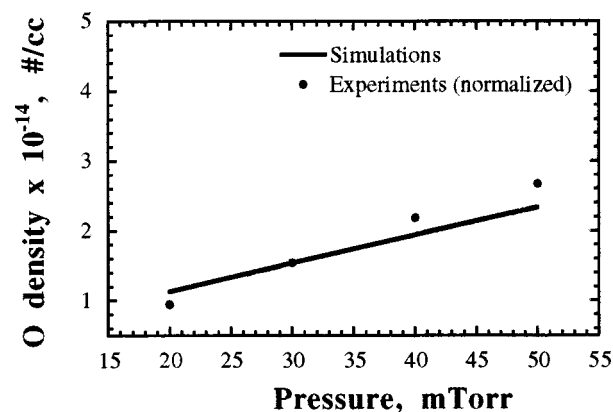

FIG. 6. Comparison of O atom concentration vs pressure in a steady state oxygen plasma at 350 W; calculation (line) and experimental data (points).

TABLE II. Base case values used in the simulation.

|	
Pressure	5 mTorr
Power (time averaged)	250 W
Duty ratio	0.5
Pulse width	100 μs
O-atom wall recombination	
Probability	0.01

malized), after the periodic steady state has been reached. Note that the time-averaged power was kept constant. Thus for a time-averaged power of 250 W and a 25% duty ratio, the power during the ''on'' part of the cycle was P_o = 1000 W.

1. Effect of duty ratio

Figures 7(a) and 7(b) show the time evolution of the electron temperature (T_e) and electron density (n_e), respectively, for four different duty ratios: 5%, 25%, 50%, and 75%. The base case values are used for all other parameters. Both the electron density and electron temperature respond to the modulated power. It is seen that the electron temperature overshoots initially reaching a peak in the first few microseconds. This is attributed to the low number density of electrons present initially which absorb the input power[33] and has been observed in experiments and simulations of Yokozawa et al.[27] in a chlorine system, and in simulations of Meyyappan for chlorine[31] and SF$_6$[34] systems. The power during the ''on'' period is higher for lower duty ratios as the time-averaged power was kept constant. Hence the peak electron temperature is higher for lower duty ratios. The peak value of T_e ranges from 6.6 eV at 5% to 4.4 eV at 75% duty ratio. As the duty ratio increases, T_e approaches the value corresponding to cw operation which is 3.6 eV. T_e rapidly decays when the power is turned off. The characteristic decay time is defined as the time taken to reach 36% (1/e) of the value when the power is turned off. The decay times range from 2.3 μs at 5% to 3 μs at 75% duty ratio. The decay rate of T_e is smaller compared to the electron concentration decay rate, as will be seen below.

Higher n_e for the lower duty ratio [Fig. 7(b)] cases is associated with higher power during the discharge on time. Similar behavior was seen in chlorine[31] and SF$_6$[34] systems. The peak n_e values vary from 6.3×10^{12}/cc with 5% duty ratio to 8.3×10^{11}/cc at 75% duty ratio. The electron concentration decays during the power off period. The n_e decay is slower compared to T_e, as the rapid decay in T_e results in decreasing Bohm velocity and hence lower electron losses.[33] The time-averaged plasma density is higher (especially at lower duty ratios) compared to the value (6.0×10^{11}/cc) obtained during cw operation for the same power, due to lower losses in the afterglow. This may have important implications from the view of processing rates. The O$^+$ (the dominant positive ion) density evolution is the same as the n_e density evolution, since the discharge is only weakly electronegative.

Figures 8 and 9 show the O$_2^M$ and O$^-$ concentrations, respectively, over a cycle at different duty ratios. Higher concentrations of O$_2^M$ and O$^-$ are obtained with higher duty
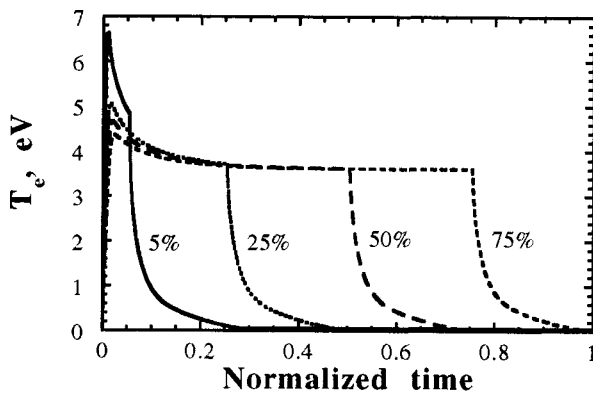
(a)
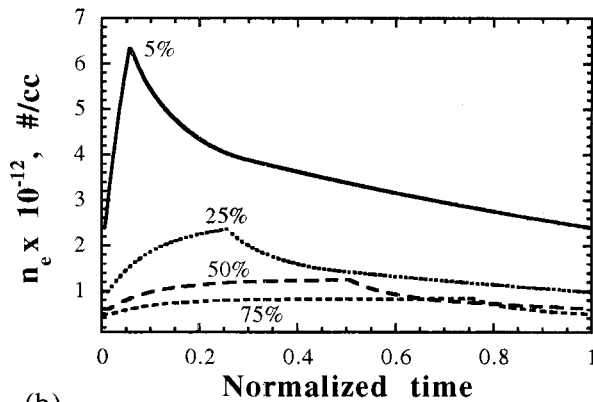
(b)

FIG. 7. Electron temperature (a) and electron density (b) during a pulse for different duty ratios. Other conditions as shown in Table II.

ratios. During the power on period, lower power is applied for higher duty ratios. Lower power results in higher concentration of both O^- and O_2^M due to lower dissociation of O_2. Slight modulation of the O_2^M density is seen only at lower duty ratios. For the base case conditions, the modulation of all neutral species except O^* was less than 6%.

The O^- density is highly modulated by the power (Fig. 9). When power is turned on (at time zero), the O^- concentration starts decreasing because of dissociation of molecular species (O_2^M and O_2) that produce negative ions. Importantly, the electron temperature starts increasing which low-
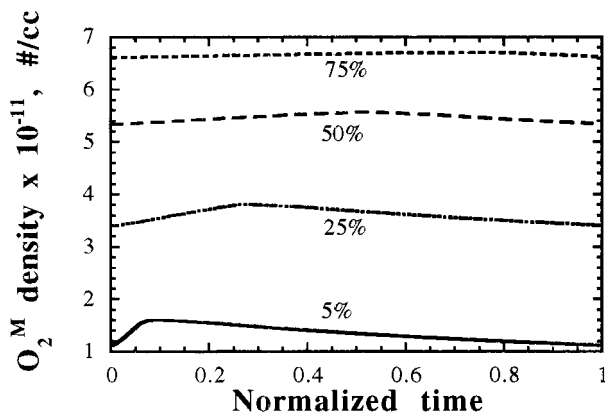
FIG. 8. O_2^M density during a pulse for different duty ratios. Other conditions as shown in Table II.
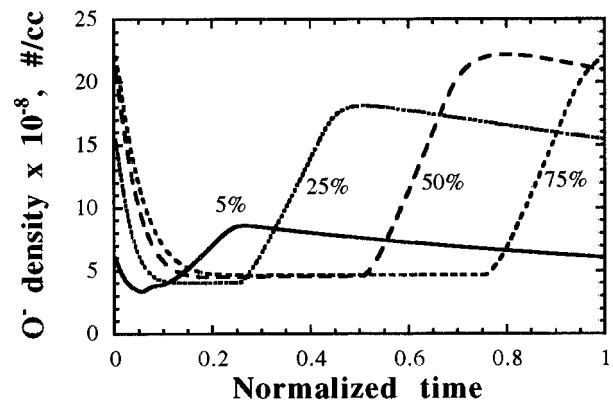

FIG. 9. O^- density during a pulse for different duty ratios. Other conditions as shown in Table II.

ers the electron attachment coefficient with O_2^M (reaction 36 in Table I). Given enough time during the active discharge phase (larger duty ratios) the negative ion concentration attains a quasisteady value. When power is turned ''off,'' the electron temperature plummets [Fig. 7(a)] and the rate coefficient of reaction 36 increases (Fig. 1) leading to an increase in the negative ion density. After some time in the afterglow, however, the electrostatic fields collapse and negative ions are capable of escaping to the walls. Thus, the negative ion density starts decreasing, after going through a peak. Recombination with positive ions also helps in removing negative ions.

The O^- flux to the walls for the base case conditions is shown in Fig. 10. During the power ''on'' part, there is no flux to the walls since negative ions are trapped by the electrostatic field of the sheath. When power is turned off, the sheath collapses resulting in O^- flux to the walls.[25] There is a time delay between power turn off (this occurs at time 0.5 in Fig. 10) and the time negative ions first appear on the wall. This corresponds to the time needed for the electron density in the discharge to decay to low enough values such that negative ions are the major negative carrier. At that point, the sheaths have collapsed and an ion–ion plasma forms.[25,32,55,56] The ''kink'' in the curve at time 0.73 occurs because the electron temperature was set equal to the constant gas temperature when it reached T_g at that point in time. Knowing the temporal evolution of O^- in the afterglow
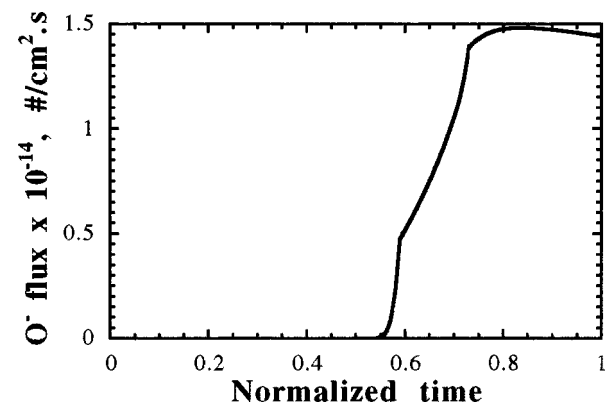

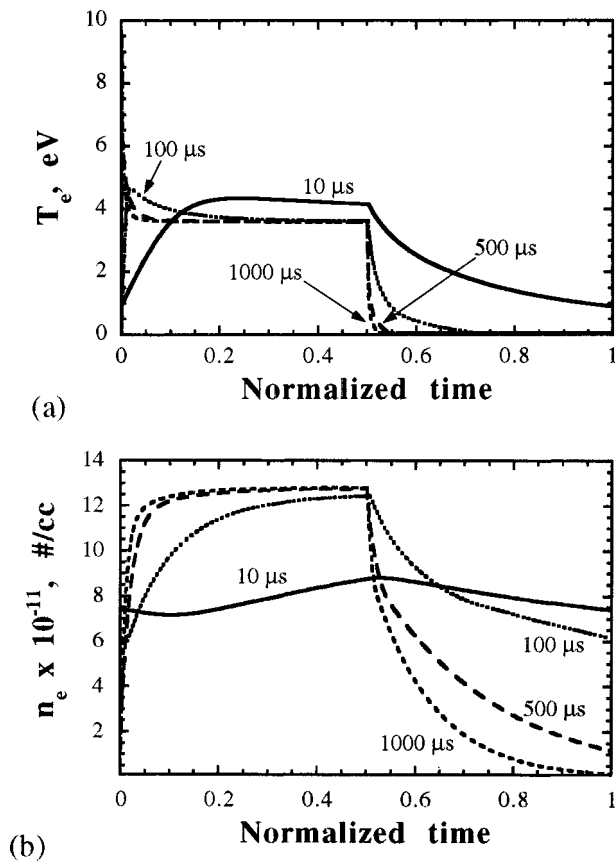FIG. 10. O^- flux at the wall for the base case conditions (Table II).

(a)

(b)

FIG. 11. Electron temperature (a) and electron density (b) during a pulse for different pulse periods. Other conditions as shown in Table II.

is important for applications requiring extraction of negative ions out of the discharge, such as charge-free semiconductor manufacturing or negative ion sources.[15–17,21,22,25,55,56]

2. Effect of pulse period

Figures 11(a) and 11(b) show T_e and n_e for pulse periods of 10 μs, 100 μs, 500 μs, and 1 ms, respectively. Base case values were used for the rest of the parameters. At low pulse periods (10 μs) the plateau electron temperature is higher and the electron density is lower. The plateau electron temperature varies from 4 eV for the 10 μs pulse period to 3.4 eV for the 1 ms pulse period. The characteristic decay time of T_e is 2.6 μs for the 10 μs case and 3 μs for the 1 ms case. No temperature spike is seen for the 10 μs case, as the electron density has not decayed significantly in the short time scale of the afterglow. Similar simulation results were obtained by Hwang and Giapis[28] for a chlorine system and Meyyappan[34] for a SF$_6$ system.

A higher plateau electron density is obtained for higher pulse periods [Fig. 11(b)] even though the T_e values are lower. Similar results were seen in the chlorine[31] and SF$_6$[34] systems. This is because the electron production exceeds the losses during the on period and the net electron production builds up further for higher pulse periods. The electron density decay times are 85 and 88 μs for the 500 μs and 1 ms pulse widths, respectively. For the 10 μs case, the maximum electron density is about 8.8×10^{11}/cc and the time is insufficient to reach the steady state. This decays to 84% of the
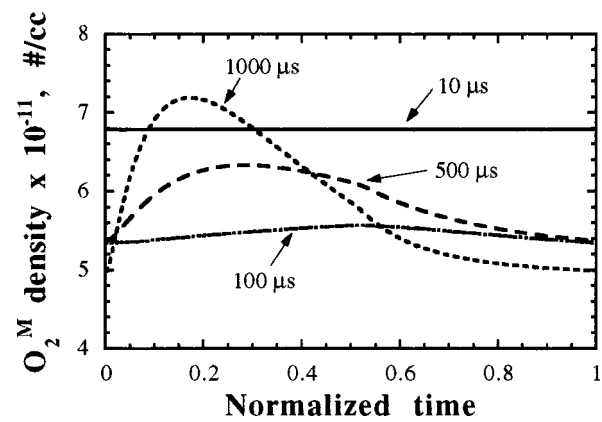

FIG. 12. O$_2^M$ density during a pulse for different pulse periods. Other conditions as shown in Table II.

maximum value at the end of the cycle. For the 100 μs case, the electron density decays to 50% of the maximum value at the end of the cycle.

Figures 12 and 13 show the O$_2^M$ and O$^-$ concentrations, respectively, for different pulse periods. The O$_2^M$ concentration for the 100 μs case is lower than the 10 μs case. This could be due to lower T_e values for the 100 μs case compared to the 10 μs case. The 500 μs and 1 ms cases show some modulation, and yield higher O$_2^M$ concentrations than the 100 μs case during the power ''on'' period. This is due to the higher electron densities and more time available for the O$_2^M$ density to build up. After the power is turned off, the O$^-$ concentration increases due to electron dissociative attachment with O$_2^M$ (Fig. 13). For the 10 μs case, there is no peak in the O$^-$ density in the afterglow. For the other three cases, the peak in O$^-$ density occurs at about 30 μs into the afterglow. Unlike the other cases, in the 1 ms case, the O$^-$ density increases initially at the start of a cycle, since the density goes down to a low value in the long afterglow time.

3. Effect of power

In the active glow, the O$^-$/n_e ratio decreases with increasing power, in agreement with the results of Stoffels et al.[36] and Lee et al.[29] Also, the O$^+$/O$_2^+$ ratio increases with increasing power, as observed by Lee et al.[29] The O$^+$ density
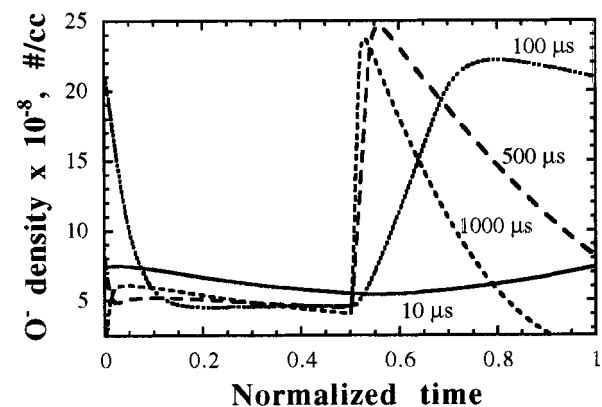

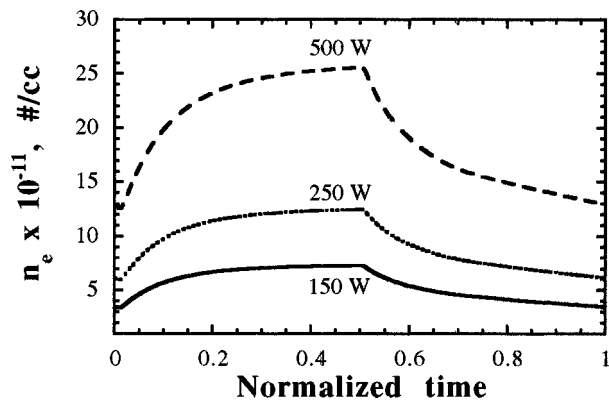FIG. 13. O$^-$ density during a pulse for different pulse periods. Other conditions as shown in Table II.
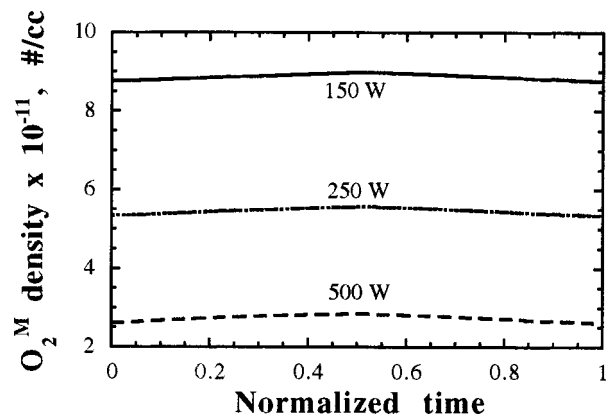
FIG. 14. Electron density during a pulse for different powers. Other conditions as shown in Table II.

FIG. 16. O$^-$ density during a pulse for different pulse powers. Other conditions as shown in Table II.

(which is the dominant positive ion) increases linearly with power. This is in agreement with experimental observations where a linear increase of the ion density with input power was found in oxygen plasmas by Keller et al.[57] in an rf ICP system, and Forster and Holber[58] in a microwave ECR system. An increase in power increases the fractional ionization rather than the electron temperature.

Figure 14 shows n_e for three different time-average powers: 150, 250, and 500 W, with the rest of the parameters being at the base values (Table II). Higher power results in higher electron density. This has been observed experimentally[37,59] in oxygen plasmas. The electron density at power off varies from 7.3×10^{11}/cc at 150 W to 2.6×10^{12}/cc at 500 W. In all three cases the electron density at the end of the cycle decreased to about 50% of the electron density at the time power was switched off. The electron density modulation is similar for different powers, as T_e was almost constant (decreased very weakly) with power. However, higher power is predicted to result in lower O_2^M and O^- densities because of more O_2 dissociation. This is shown in Figs. 15 and 16, respectively. The O_2^M density does not follow the power modulation, while the modulation of the O^- density is higher at lower powers. The time in the afterglow (after power turn off) at which the peak O^- density occurs decreases with power, from 32 μs at 150 W to 25 μs at 500 W. In contrast to Fig. 16, Hayashi and Kadota[37] obtained

experimentally higher O^- concentrations at higher power. We have no explanation for this behavior at this time. In another study, Stoffels et al.,[36] using a capacitively coupled cw oxygen plasma, found that the O^- concentration was independent of power, even though the electron concentration increased by a factor of 10 as power was increased.

4. Effect of pressure

Figures 17(a) and 17(b) show T_e and n_e, respectively, for three different pressures, 5, 20, and 40 mTorr, with the rest of the parameters being at the base case values. A decrease in T_e with pressure has been experimentally measured

(a)

FIG. 15. O_2^M density during a pulse for different powers. Other conditions as shown in Table II.
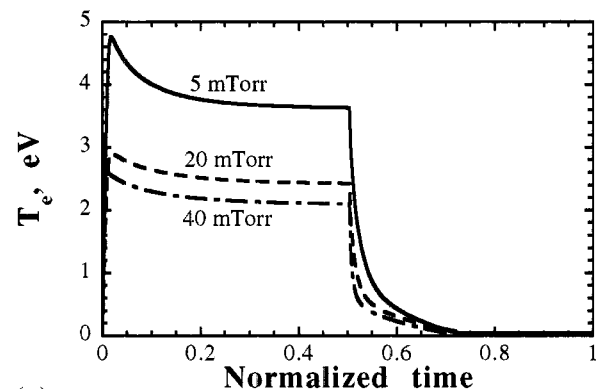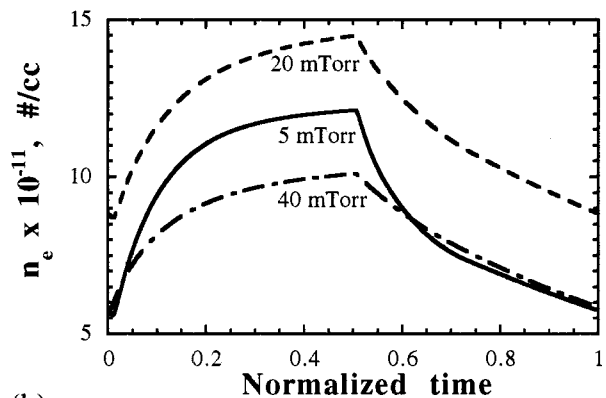
(b)

FIG. 17. Electron temperature (a) and electron density (b) during a pulse for different pressures. Other conditions as shown in Table II.
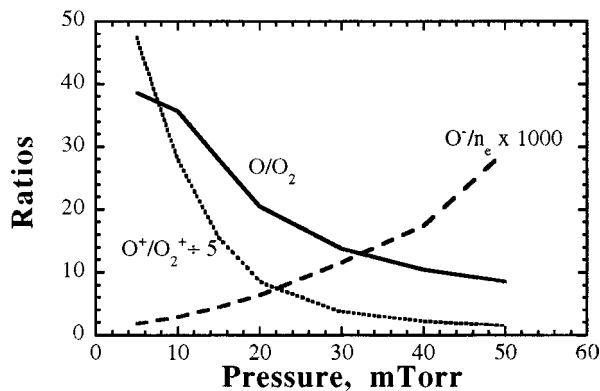
FIG. 18. Species density ratios as a function of pressure in a steady state plasma. Other applicable conditions as shown in Table II.

FIG. 19. O_2^M density during a pulse for different pressures. Other conditions as shown in Table II.

by Forster and Holber[58] in an ECR oxygen plasma. The electron density has a peak with pressure; it decreases at low pressures due to a decrease in the number of particles available for ionization, while it decreases at higher pressures due to lower T_e which results in a reduction in the ionization rate coefficient.

Increasing pressure results in increasing densities of both O_2 and O in the active plasma (see also Fig. 6). An increasing O density with pressure has been measured by Tserepi and Miller[38] in a parallel plate rf oxygen discharge. Figure 18 shows the O/O_2 ratio for a steady-state cw plasma for different pressures. Other conditions were those of the base case. Increasing pressure results in lower fractional dissociation as seen from the decreasing O/O_2 ratio. O^+ is the dominant positive ion as O is the dominant neutral in the highly dissociated system. The O^+/O_2^+ ratio decreases with pressure while the O_2^+ density increases with pressure and the O^+ density shows a weak peak at 30 mTorr (not shown). Keller et al.[57] found the ion density to decrease with pressure in the range 1–30 mTorr in an ICP. Apparently, in this pressure range, the effect of decreasing T_e with pressure was dominant resulting in lower ionization. Also shown in Fig. 18 is the calculated O^-/n_e density ratio. Higher O_2 density at higher pressures results in higher O_2^M density and consequently higher O^- density. The O^-/n_e ratio increases with pressure, while n_e reaches a peak at 30 mTorr (corresponding to the peak in O^+ density, not shown). The behavior of O/O_2, O^+/O_2^+, and O^-/n_e with pressure is in agreement with the observations of Lee et al.[29] The simulations of Shibata et al.[50] showed a peak in O_2^+ (dominant positive ion) density and those of Stoffels et al.[36] showed a peak in n_e with pressure.

Figures 19 and 20 show the O_2^M and O^- densities at three different pressures, 5, 20, and 40 mTorr. Higher O_2^M densities are obtained at higher pressures. The O_2^M density does not show any significant modulation at any of the three pressures. The O^- density rapidly decreases within the first 7–15 μs after power is turned on ($t=0$). This is due to O_2^M dissociation and also formation of more O^+ which neutralizes O^-. As discussed before, the O^- density increases in the afterglow initially due to dissociative attachment and lower neutralization losses with O^+ and then decreases slowly due to wall losses and ion–ion neutralization. In the afterglow,
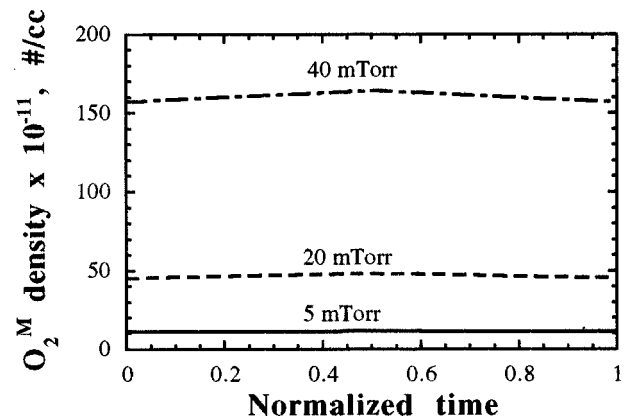
the peak O^- densities occur at 30, 21, and 16 μs after power is turned off for the 5, 20, and 40 mTorr cases, respectively. Also, the ratio of the peak O^- density to the density at power turn off decreases from 4.8 to 3.6 in the same pressure range.

V. CONCLUSIONS

Hayashi and Kadota[37] measured a large increase in the negative O^- concentration in the afterglow of a high density pulsed oxygen discharge. Dissociative attachment of electrons with ground state O_2 and O_2^* ($a\,^1\Delta_g$) metastables cannot account for the increase in O^- density in the afterglow. In this work, new chemistry involving the 4 eV $O_2^M(A\,^3\Sigma_u^+ + C\,^3\Delta_u + c\,^1\Sigma_u^-)$ metastables, as suggested by Hayashi and Kadota,[37] was used to simulate a high density power-modulated (pulsed) oxygen discharge, using a spatially averaged (well mixed) reactor model. The temporal behavior of the O^- and electron density in the afterglow was captured by the simulation. Also, the behavior of the predicted oxygen atom concentration as a function of pressure in a steady-state plasma was similar to the experimental results. However, the model predicted a decrease in O^- density with power which is opposite to the trend observed experimentally. A parametric analysis was conducted to study the effect of operating conditions on the plasma properties and species densities. The wall recombination probability of oxygen atoms affected
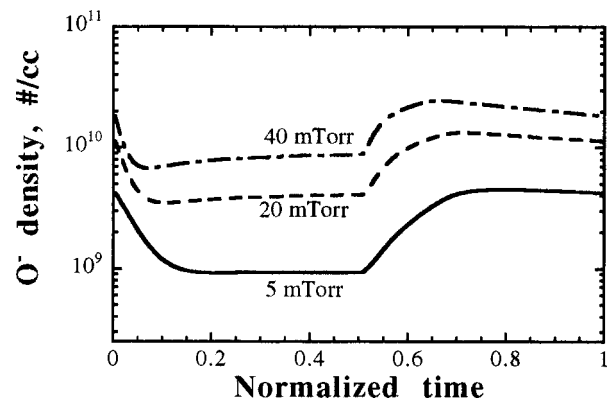
FIG. 20. O^- density during a pulse for different pressures. Other conditions as shown in Table II.

J. Appl. Phys., Vol. 87, No. 12, 15 June 2000

Panda, Economou, and Meyyappan   8333

the O^- density drastically. Of all species, the O^- density showed the strongest time modulation during a pulse. The trends in O^- density with pressure and power were the same as for the O_2^M density. For the conditions studied, the maximum O^- density in the afterglow increased with pressure, decreased with power, and showed a maximum with pulse period. The time in the afterglow at which the peak O^- density occurred decreased with pressure and power, and was independent of the pulse period. Knowing the temporal evolution of O^- in the afterglow is important for applications requiring extraction of negative ions out of the discharge, such as charge-free semiconductor processing and negative ion sources.

ACKNOWLEDGMENTS

[1] Y. Watanabe, M. Shiratani, Y. Kubo, I. Ogawa, and S. Ogi, Appl. Phys. Lett. **53**, 1263 (1988).

[2] Y. Watanabe, M. Shiratani, and H. Maniko, Appl. Phys. Lett. **57**, 1616 (1990).

[3] L. J. Overzet and J. T. Verdeyen, Appl. Phys. Lett. **48**, 695 (1986).

[4] A. Bouchoule, A. Plain, L. Boufendi, J. Ph. Blondeau, and C. Laure, J. Appl. Phys. **70**, 1991 (1991).

[5] R. W. Boswell and R. K. Porteous, J. Appl. Phys. **62**, 3123 (1987).

[6] R. W. Boswell and D. Henry, Appl. Phys. Lett. **47**, 1095 (1985).

[7] C. Grabowski and J. M. Gahl, J. Appl. Phys. **70**, 1039 (1991).

[8] V. J. Law, M. Tewordt, D. C. Clary, and G. A. C. Jones, J. Vac. Sci. Technol. B **11**, 2262 (1993).

[9] V. J. Law, N. St. J. Braithwaite, S. G. Ingram, D. C. Clary, and G. A. C. Jones, J. Vac. Sci. Technol. B **12**, 3337 (1994).

[10] S. Samukawa, Jpn. J. Appl. Phys., Part 1 **32**, 6080 (1993).

[11] S. Samukawa, Jpn. J. Appl. Phys., Part 1 **33**, 2133 (1994).

[12] S. Samukawa and S. Furoya, Appl. Phys. Lett. **63**, 2044 (1993).

[13] K. Takahashi, M. Hori, and T. Goto, Jpn. J. Appl. Phys., Part 2 **32**, L1088 (1993).

[14] N. Fujiwara, T. Maruyama, and M. Yoneda, Jpn. J. Appl. Phys., Part 1 **35**, 2450 (1996).

[15] S. Samukawa, Appl. Phys. Lett. **64**, 3398 (1994); **68**, 316 (1996).

[16] S. Samukawa and K. Terada, J. Vac. Sci. Technol. B **12**, 3300 (1994); S. Samukawa and T. Tsukuda, J. Vac. Sci. Technol. A **15**, 643 (1997); S. Samukawa, H. Ohtake, and T. Mieno, J. Vac. Sci. Technol. A **14**, 3049 (1996).

[17] M. B. Hopkins and K. N. Mellon, Phys. Rev. Lett. **67**, 449 (1991).

[18] S-K. Park and D. J. Economou, J. Electrochem. Soc. **137**, 2103 (1990).

[19] S-K. Park and D. J. Economou, J. Electrochem. Soc. **137**, 2624 (1990).

[20] P. Jiang, D. J. Economou, and C. B. Shin, Plasma Chem. Plasma Process. **15**, 383 (1995).

[21] L. J. Overzet, J. Vac. Sci. Technol. A **11**, 1114 (1993).

[22] L. J. Overzet, Y. Lin, and L. Luo, J. Appl. Phys. **72**, 5579 (1992).

[23] I. Peres and L. C. Pitchford, J. Appl. Phys. **78**, 774 (1995).

[24] D. P. Lymberopoulos, V. I. Kolobov, and D. J. Economou, J. Vac. Sci. Technol. A **16**, 564 (1998).

[25] V. Midha and D. J. Economou, Plasma Sources Sci. Technol. (submitted).

[26] H. B. Smith, C. Charles, R. W. Boswell, and H. Kuwahara, J. Appl. Phys. **82**, 561 (1997).

[27] A. Yokozawa, H. Ohtake, and S. Samukawa, Jpn. J. Appl. Phys., Part 1 **35**, 2433 (1996).

[28] G. S. Hwang and K. P. Giapis, Jpn. J. Appl. Phys., Part 1 **37**, 2291 (1998).

[29] C. Lee, D. B. Graves, M. A. Lieberman, and D. W. Hess, J. Electrochem. Soc. **141**, 1546 (1994).

[30] M. Meyyappan and T. R. Govindan, Vacuum **47**, 215 (1996).

[31] M. Meyyappan, J. Vac. Sci. Technol. A **14**, 2122 (1996).

[32] S. Ashida and M. A. Lieberman, Jpn. J. Appl. Phys., Part 1 **36**, 854 (1997).

[33] S. Ashida, C. Lee, and M. A. Lieberman, J. Vac. Sci. Technol. A **13**, 2498 (1995).

[34] M. Meyyappan, Jpn. J. Appl. Phys., Part 1 **36**, 4820 (1997).

[35] R. L. Bersin, Solid State Technol. **13**, 39 (1970); B. R. Soller, R. F. Shuman, and R. R. Ross, J. Electrochem. Soc. **131**, 1353 (1984).

[36] E. Stoffels, W. W. Stoffels, D. Vender, M. Kando, G. M. W. Kroesen, and F. J. de Hoog, Phys. Rev. E **51**, 2425 (1995).

[37] D. Hayashi and K. Kadota, J. Appl. Phys. **83**, 697 (1998).

[38] A. D. Tserepi and T. A. Miller, J. Appl. Phys. **77**, 505 (1995); J. P. Booth and N. Sadeghi, *ibid.* **70**, 611 (1991).

[39] E. Meeks and J. W. Shon, IEEE Trans. Plasma Sci. **23**, 539 (1995).

[40] M. Meyyappan and T. R. Govindan, *SAMPR: A Computer Code for Simple Analysis of Materials Processing Reactors* (NASA Research, CA, 1997).

[41] C. Lee and M. A. Lieberman, J. Vac. Sci. Technol. A **13**, 368 (1995).

[42] M. A. Lieberman and A. J. Lichtenberg, *Principles of Plasma Discharges and Materials Processing* (Wiley, New York, 1994), p. 255.

[43] P. D. Burrow, J. Chem. Phys. **59**, 4922 (1973).

[44] D. Hayashi and K. Kadota, Jpn. J. Appl. Phys., Part 1 **38**, 225 (1999).

[45] D. Teillet-Billy, L. Malegat, J. P. Gauyacq, R. Abouaf, and C. Benoit, J. Phys. B **22**, 1095 (1989).

[46] Y. Itikawa, A. Ichimura, K. Onda, K. Sakimoto, K. Takayanagi, Y. Hatano, M. Hayashi, H. Nishimura, and S. Tsurubuchi, J. Phys. Chem. Ref. Data **18**, 23 (1989).

[47] P. J. Chantry, J. Appl. Phys. **62**, 1141 (1987).

[48] G. Gousset, C. M. Ferreira, M. Pinheiro, P. A. Sa, M. Touzeau, M. Vialle, and J. Loureiro, J. Phys. D: Appl. Phys. **24**, 301 (1991).

[49] A. T. Bell, *Techniques and Applications of Plasma Chemistry* (Wiley, New York, 1974), pp. 28 and 29.

[50] M. Shibata, N. Nakano, and T. Makabe, J. Appl. Phys. **80**, 6142 (1996).

[51] J. Matsushita, K. Sasaki, and K. Kadota, Jpn. J. Appl. Phys., Part 1 **7B**, 4747 (1997).

[52] E. J. H. Collart, J. A. G. Baggerman, and R. J. Visser, J. Appl. Phys. **70**, 5278 (1991).

[53] J. M. Cook and B. W. Benson, J. Electrochem. Soc. **130**, 2459 (1983).

[54] A. Schwabedissen, E. C. Benck, and J. R. Roberts, Phys. Rev. E **55**, 3450 (1997).

[55] M. Shibata, N. Nakano, and T. Makabe, J. Appl. Phys. **77**, 6181 (1995).

[56] B. A. Smith and L. J. Overzet, Plasma Sources Sci. Technol. **8**, 82 (1999); D. Smith, A. G. Dean, and N. G. Adams, J. Phys. D: Appl. Phys. **7**, 1944 (1974).

[57] J. H. Keller, J. C. Forster, and M. C. Barnes, J. Vac. Sci. Technol. A **11**, 2487 (1989).

[58] J. Forster and W. Holber, J. Vac. Sci. Technol. A **7**, 899 (1989).

[59] O. A. Popov, J. Vac. Sci. Technol. A **7**, 894 (1989).